

Time-bin encoded quantum key distribution over 120 km with a telecom quantum dot source

Jipeng Wang¹, Joscha Hanel¹, Zenghui Jiang¹, Raphael Joos², Michael Jetter², Eddy Patrick Rugeramigabo¹, Simone Luca Portalupi², Peter Michler², Xiao-Yu Cao³, Hua-Lei Yin^{3,4}, Shan Lei⁵, Jingzhong Yang^{1,*}, Michael Zopf^{1,6}, and Fei Ding^{1,6,*}

¹Institut für Festkörperphysik, Leibniz Universität Hannover, Appelstraße 2, 30167 Hannover, Germany

²Institut für Halbleiteroptik und Funktionelle Grenzflächen, Center for Integrated Quantum Science and Technology (IQST) and SCoPE, University of Stuttgart, Allmandring 3, 70569 Stuttgart, Germany

³National Laboratory of Solid State Microstructures and School of Physics, Collaborative Innovation Center of Advanced Microstructures, Nanjing University, Nanjing 210093, China

⁴Department of Physics and Beijing Key Laboratory of Opto-electronic Functional Materials and Micro-nano Devices, Key Laboratory of Quantum State Construction and Manipulation (Ministry of Education), Renmin University of China, Beijing, 100872, China

⁵Information Materials and Intelligent Sensing Laboratory of Anhui Province, Institutes of Physical Science and Information Technology, Anhui University, Hefei, China

⁶Laboratorium für Nano- und Quantenengineering, Leibniz Universität Hannover, Schneiderberg 39, 30167 Hannover, Germany

*jingzhong.yang@fkp.uni-hannover.de

*fei.ding@fkp.uni-hannover.de

ABSTRACT

Quantum key distribution (QKD) with deterministic single photon sources has been demonstrated over intercity fiber and free-space channels. The previous implementations relied mainly on polarization encoding schemes, which are susceptible to birefringence, polarization-mode dispersion and polarization-dependent loss in practical fiber networks. In contrast, time-bin encoding offers inherent robustness and has been widely adopted in mature QKD systems using weak coherent laser pulses. However, its feasibility in conjunction with a deterministic single-photon source has not yet been experimentally demonstrated. In this work, we construct a time-bin encoded QKD system employing a high-brightness quantum dot (QD) single-photon source operating at telecom wavelength. Our proof-of-concept experiment successfully demonstrates the possibility of secure key distribution over fiber link of 120 km, while maintaining extraordinary long-term stability over 6 hours of continuous operation. This work provides the first experimental validation of integrating a quantum dot single-photon source with time-bin encoding in a telecom-band QKD system. In addition, it demonstrates the highest secure key rate among the time-bin QKDs based on single-photon sources. This development signifies a substantial advancement in the establishment of a robust and scalable QKD network based on solid-state single-photon technology.

Introduction

Quantum key distribution (QKD) offers a practical approach to realize physical-level confidentiality for the sharing of secret keys in a communication network^{1–4}. Since the first BB84 protocol⁵, significant progress has been made to bridge the gap between the theoretically unconditional security and practical implementation^{6–8}. Among the proposed methods, the decoy-state protocol plays a crucial role in practical QKD systems^{9–12}. Using weak coherent pulses (WCPs) in the decoy-state protocol enables a secure and cost-effective implementation. As a result, it has been widely adopted in national and commercial QKD networks^{13–18}. Despite its success, the performance of decoy-state QKD with WCPs as approximations to ideal single-photons remains fundamentally constrained. The probability of true single-photon emission is upper-bounded by the Poisson statistics of WCPs^{19–21}, and additional modulation processes required to implement the decoy protocol may introduce complexity and side-channel vulnerabilities^{22–25}. These limitations have motivated the pursuit of genuine single-photon sources (SPSs) for QKD.

Semiconductor quantum dots (QDs) embedded in nanophotonic structures offer on-demand, high-purity single-photon emission with high efficiency^{26–29}. Recent works have demonstrated the feasibility of using QDs as SPSs in QKD systems, both over fiber^{30–36} and free-space^{37–39} channels. In particular, telecom-band QDs with Purcell enhancement⁴⁰ can provide

high-brightness photons suitable for intercity fiber communication⁴¹, making them promising candidates for integration into practical QKD systems. Most existing QD-based QKD demonstrations rely on polarization encoding^{36,42,43}, but such schemes are highly sensitive to polarization-mode dispersion (PMD) and birefringence in optical fibers^{44–48}. In contrast, time-bin encoding, where qubits are encoded in the temporal position of single photons, offers intrinsic stability against such channel attacks even without any active compensation. While time-bin encoding has been widely demonstrated using coherent-state or entangled-photon sources^{49–54}, its implementation with deterministic QD-based SPSs remains largely unexplored.

Pioneering studies have utilized QDs for phase-encoding QKD^{30,32}, where asymmetric Mach-Zehnder interferometers (AMZIs) are used to create time-bin-like phase states. However, in those cases, the time-bin is not directly employed for key generation, and long-term stability tests are lacking. Entanglement-based QKD systems have also been explored^{55–60}, but they require complex state preparation techniques and are less practical for compact deployments. To date, there has been no demonstration of a QKD system employing genuine time-bin-encoding with deterministic single photons from quantum dots, especially at long distances.

In this work, we present a self-stabilized, time-bin encoded QKD system based on a deterministic telecom-wavelength quantum dot source⁴⁰. To minimize system complexity and loss, we adopt a single phase modulator for preparing three quantum states: two time-bin basis states ($|Z_0\rangle$, $|Z_1\rangle$) and one phase-basis state ($|X_0\rangle$), assuming $|X_0\rangle$ shares the same error rate as $|X_1\rangle$ in the conventional BB84 protocol^{50,61}. The system is operated continuously for 6 hours, highlighting the intrinsic robustness of the time-bin scheme enabled by the system including the Sagnac interferometer (SNI), active feedback control, etc. Finally, we achieved a secure key bits (SKB) per pulse of 2×10^{-7} over a 120 km fiber spool. This result confirms the feasibility of integrating quantum dot single-photon sources into stable and field-deployable time-bin QKD systems, marking an important step toward scalable, quantum-secure communication networks.

Results

Overview of the experimental scheme

The three time-bin states of the polarized single photons are generated using an AMZI configuration involving a SNI. In this configuration, the input beam splitter of the standard AMZI is replaced with a fiber-based optical circulator (Cir), as shown in the left panel of Fig. 1a, so that the single photons are first guided into the SNI passing through BS_1 . In the SNI structure, a $LiNbO_3$ phase modulator (PM, Rofea Optoelectronics, ROF-PM-UV) is intentionally placed in an unbalanced position. Single photons arriving at the PM along the clockwise (\odot) path at the time $t_0 + \Delta$ experience an additional time delay of Δ (half of the single-photon repetition period), compared to those arriving along the counterclockwise (\ominus) path at the time t_0 .

In this experiment, we intentionally setup Δ to 6.5 ns as shown in Fig. 1b, considering the excitation repetition rate for the single photons is $f_{rep} = 75.947$ MHz. A correlation between the phase and the time of the photons arriving at the PM can be created by applying a sequence of two voltages to the PM within each single-photon period ($1/f_{rep} \approx 13.17$ ns). Within one single-photon period, one of the voltages in the set $\{0, V_\pi, V_{\pi/2}\}$ is applied to the PM at t_0 over the first time slot, while no voltage is applied to PM at $t_0 + \Delta$ for the second time slot. A phase of θ_1 for each single photon can be actively determined, leading to the generation of single-photon path states from the SNI due to the single-photon interference,

$$|\Phi\rangle_{SNI} = ie^{i\frac{\theta_1}{2}} \left(-\sin \frac{\theta_1}{2} \cdot |S\rangle + \cos \frac{\theta_1}{2} \cdot |L\rangle \right) \quad (1)$$

The states $|S\rangle$ and $|L\rangle$ represent the quantum states of the short and long paths that the photons chose between the BS_1 and BS_2 . The single photons with the state $|L\rangle$ enter the green path of the $AMZI_1$ and go through the Cir (through port 2→3) in Fig. 1(a), giving a time delay of Δ_1 in comparison with the state $|S\rangle$. This results in the equal time separation between the early $|e\rangle$ and late $|l\rangle$ photons after the $AMZI_1$. Assuming the transmitted and reflected single photons from the output port of BS_2 corresponds to the $|L\rangle$ and $|S\rangle$ single-photon states, the time-bin state of a photon from $AMZI_1$ is,

$$|\Psi\rangle_{AMZI_1} = \frac{1}{\sqrt{2}} e^{i\frac{\theta_1}{2}} \left(\sin \frac{\theta_1}{2} \cdot |e\rangle + i \cos \frac{\theta_1}{2} \cdot |l\rangle \right) \quad (2)$$

with $1/\sqrt{2}$ indicating the amplitude of state from one port, and i the phase shift of $\pi/2$ for the $|S\rangle$ -state photons upon reflection relative to transmission at BS_2 . In this work, a single output port is used for key transmission. Figure 1c shows the sketch of correlation histograms between the single-photon triggering signals and the three time-bin states $|Z_0\rangle = |l\rangle$, $|Z_1\rangle = |e\rangle$ and $|X\rangle = 1/\sqrt{2}(|e\rangle + i|l\rangle)$, corresponding to the voltage levels of $\{0, V_\pi, V_{\pi/2}\}$ shown in Fig. 1b, respectively. Within a single-photon period, three time windows $\{W_1, W_2, W_3\}$ are defined each with a range of $\Delta_1 = 4.3$ ns. Coincidences that occur solely in W_1 and W_2 indicate the presence of the $|e\rangle$ and $|l\rangle$ photons, respectively. The probabilities of 50 % for each W_1 and W_2 suggests the successfully encoded of $|X_0\rangle$ state.

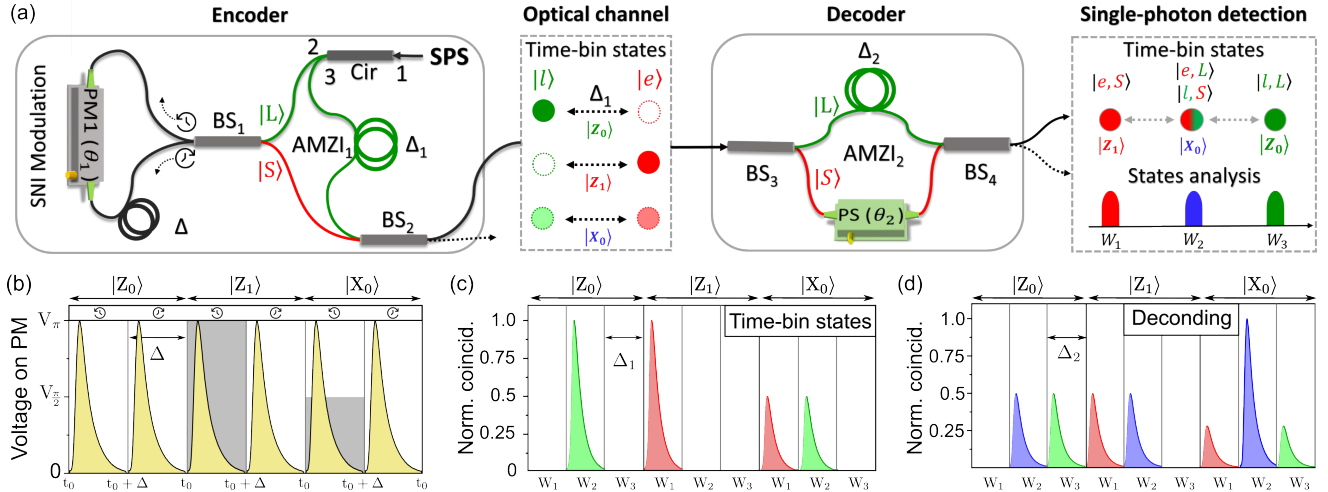


Figure 1. Encoding and decoding schemes of time-bin QKD. (a) Encoder for preparing three time-bin states. Single photons emitted by the QD pass through the port 1→2 of the optical circulator (Cir) and then through the beam splitter 1 (BS_1). A phase of θ_1 in the set $\{0, \pi/2, \pi\}$ is randomly encoded to the single photons via an electro-optic phase modulator (PM) within the SNI. Three single-photon path state $|L\rangle$ (green), $1/\sqrt{2}(|S\rangle + |L\rangle)$ and $|S\rangle$ (red) that are generated from the single-photon interference due to the phase θ_1 , are translated into three time-bin states ($|Z_0\rangle, |Z_1\rangle, |X_0\rangle$) after BS_2 . After the transmission of the single photons through the optical channel, a phase shifter (PS) involved $AMZI_2$ at the decoder interpret the time-bin states to be measurable using the single-photon detection. The solid lines of BS_2 and BS_4 outputs denote the active port being used in the scheme. Three states $|Z_1\rangle, |Z_0\rangle, |X_0\rangle$ can be measured corresponding to the histograms within the time windows W_1 (red), W_2 (blue) and W_3 (green) of the single-photon correlation measurement. (b) Sketch of the active phase control of single photons (yellow) via the PM in SNI configuration. Each single-photon period is divided into two time slots, considering the different arrival time of single photons at PM along superposition of clockwise (\odot) and counter-clockwise (\ominus) paths with a time delay of Δ . One constant voltage in the set $\{0, V_\pi, V_{\pi/2}\}$ (gray background) is applied to the PM to tune the phase of photons at the first time slot of each single-photon period, resulting in the generation of different path states from the SNI. (c) Sketch of single-photon correlation histograms with three time-bin states ($|Z_0\rangle, |Z_1\rangle, |X_0\rangle$) after the encoder. The time delay of Δ_1 from $AMZI_1$ is revealed as the time delay between early $|e\rangle$ and late $|l\rangle$ photons. (d) Sketch of the time-bin states correlation histograms after the $AMZI_2$ decoder.

To decode the time-bin states, an AMZI with an internal time delay of $\Delta_2 = \Delta_1$ and a phase shifter (PS, Luna Innovation, FPS-001) is employed. For simplicity, we ignore the global phase induced by the quantum channel in between the encoder and decoder, and exemplifying the phase $\theta_2 = \pi/2$ from the PS. Then the single-photon state from output 1 of the $AMZI_2$ can be expressed as follows,

$$\begin{aligned} |\Psi\rangle_{AMZI_2} &= R_{AMZI} \cdot |\Psi\rangle_{AMZI_1} \\ &= \frac{1}{2\sqrt{2}} e^{i\frac{\theta_1}{2}} \left(-i \sin \frac{\theta_1}{2} |e, S\rangle + \sin \frac{\theta_1}{2} |e, L\rangle + \cos \frac{\theta_1}{2} |l, S\rangle + i \cos \frac{\theta_1}{2} |l, L\rangle \right) \end{aligned} \quad (9)$$

where the R_{AMZI} is operation gate of $AMZI_2$ for the single-photon state (see details in the methods). Here we assume that the phase shift of $\pi/2$ applied to single-photon states, when the $AMZI_2$ short path and active output port corresponds to the reflected photons from the BS_3 and BS_4 , respectively. Figure 1d represent the detection of a single photon at a set of given time windows $\{W_1, W_2, W_3\}$ corresponding to three cases after $AMZI_2$,

1. The early photon goes through the short path $|e, S\rangle$;
2. The early photon goes through the long path $|e, L\rangle$ or the late photon goes through the short path $|l, S\rangle$;
3. The late photon goes through the long path $|l, L\rangle$;

In the the Equ. 3, the first term indicates the global phase induced by PM, while the square of the factors relevant to θ_1 in the second term denote the probability of photons located in the corresponding time windows. The sketch of correlation histograms in Fig. 1d illustrates the normalized probabilities of the above cases when the phase θ_1 , encoded by the PM, is set to

$\{0, V_\pi, V_{\pi/2}\}$. In our time-bin-based QKD scheme, we implement the sifting with the raw keys by measuring the correlated photonic states $\{Z_1, X_0, Z_0\}$ that are correlated with the photons arriving at the windows of $\{W_1, W_2, W_3\}$, respectively.

Experimental setup

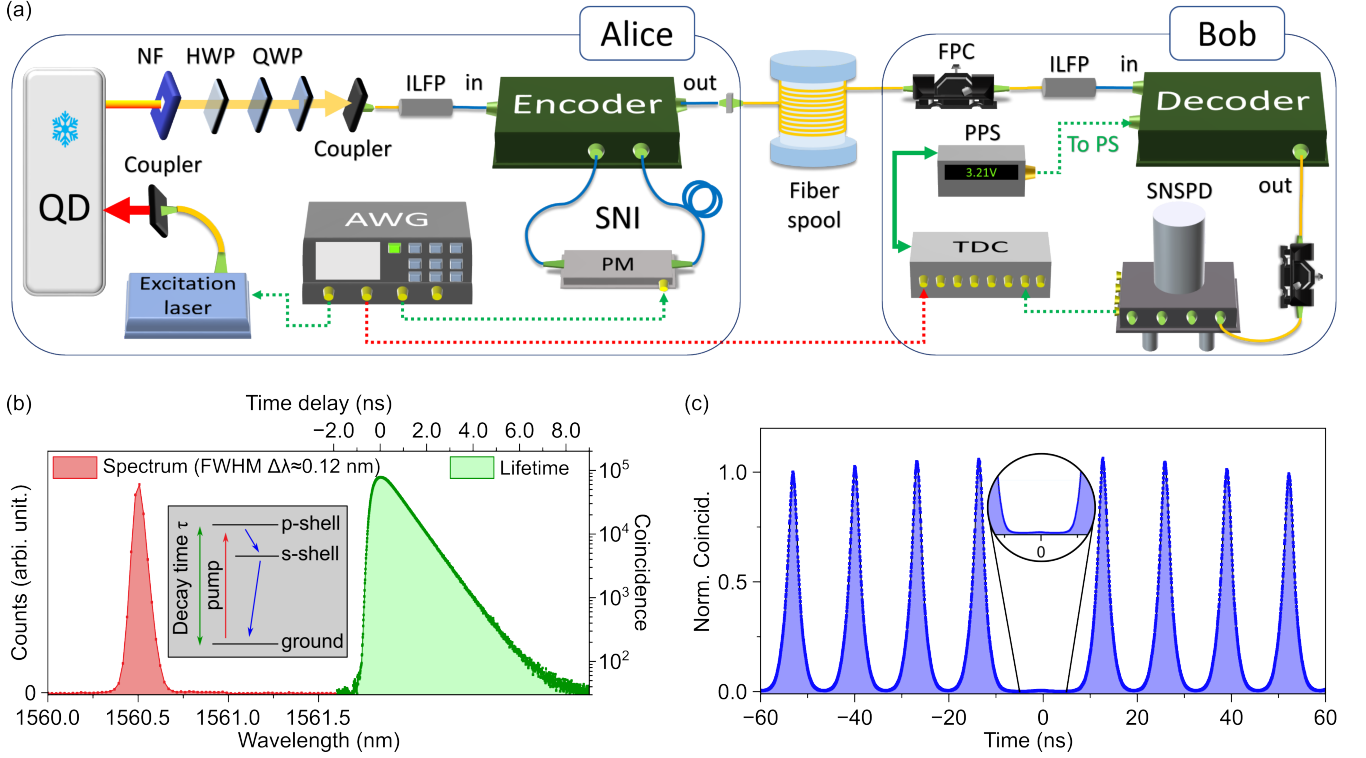


Figure 2. (a) Fiber-coupled excitation pulse laser, triggered by the arbitrary wave-function generator (AWG), is used to excite the telecom QD loaded in the cryostat. The emitted single photons are extracted from the laser using a notch filter. Then, single photons are coupled to the in-line fiber polarizer (ILFP), through a series of free-space half- and quarter- waveplates (HWP and QWP) for the polarization control. The PM inside the encoder is synchronized with the excitation laser via the AWG, and randomly generate three single-photon time-bin states. The time-bin qubits are decrypted at the receiver setup from Bob, which consists of a decoder, superconducting nanowire single-photon detector (SNSPD), and a time-to-digital converter (TDC). FPC, fiber polarization controller; PPS, programmable power source. (b) The photoluminescence spectrum and time-resolved lifetime histogram (logarithm scale) of the single-photon emissions from the QD. The inset shows the decay process of the p-shell excitation within the QD band structure. (c) Normalized second-order autocorrelation histogram for the single photons from the trion state emissions with the inset showing the zoomed-in view of the central peak.

Figure 2 shows a sketch of the experimental setup for time-bin QKD using telecom single photons from the semiconductor QD. The circular Bragg grating photonic device containing the QD, is loaded in a cryostat at a temperature of 3.57 K. A pulsed laser with a repetition rate of $f_{rep} = 75.947$ MHz that is synchronized with an arbitrary wave-function generator (AWG, Active Technologies, AWG5064) is used to excite the p-shell of the positive trion state of the QD, resulting in the single-photon emissions at 1560.6 nm (Fig. 2a). The total decay time is extracted by fitting the time-resolved QD emission in a three-level system and is found to be $\tau = 1018$ ps. In a time-bin QKD system, employing the photonic resonant structure can reduce the lifetime and compromise the inherent limit of the repetition rates, which is half that of QKDs based on other photonic degrees of freedom, e.g., polarization. To evaluate the influence of the single-photon purity on QKD, we performed an autocorrelation measurement using a Hanbury Brown and Twiss setup and extract a blinking-corrected $g^2(0) = 0.85\%$ from the histogram (Fig. 2c) without any temporal filter applied to the coincidence count integration ($\tau = 1/f_{rep}$).

Before the time-bin encoder, the single photons are first polarized by an in-line fiber polarizer (ILFP) to align their polarization with the axis of the fiber optics, i.e., PM. In the SNI configuration, the phase control with the PM is implemented by an AWG that delivers squared modulation signals in pair with a clock rate locked to the excitation laser. Three voltage gaps $\{0, 1.6\text{ V}, 3.2\text{ V}\}$ corresponding to $\{0, V_{\pi/2}, V_{\pi}\}$ within each pair are applied to PM over the first time slot to generated the three time-bin states. In the actual experiment, a 16-bit repeating sequence with these random voltages are applied to the PM

for the states of $\{X_0, Z_1, Z_0, X_0, Z_0, Z_1, X_0, Z_1, Z_0, X_0, Z_0, Z_1, X_0, Z_0, Z_1, Z_1\}$, with number of bits $\{5, 6, 5\}$ for $\{Z_0, Z_1, X_0\}$. The encrypted single photons are then sent to the receiver setup through the variable-length fiber spools. Similar to the transmitter at Alice, the receiver at Bob uses an ILFP to ensure the alignment of the photon's polarization with the axis of the fiber optics in the decoder. A fiber polarization controller is placed in front to compensate the polarization drift from the fiber channel. Additionally, a programmable power source (PPS, Siglent Technologies, SPD3303) controls the PS in the decoder to actively stabilize the phase between the $AMZI_2$'s arms by minimizing the quantum bit error rate (QBER) of the system. Eventually, the arrival times of the single photons are registered by a superconducting nanowire single-photon detector (SNSPD), followed by a time-to-digital converter synchronized with the AWG.

Evaluation of the QKD performance

As the figure-of-merit for QKDs, the secure key rate (SKR) R_{secure} from the three time-bin states, is emulated in the finite-key regime with the multiplicative Chernoff bound³¹,

$$R_{secure} = \left[\frac{N_{R,nmp}^Z}{N_{sum}} (1 - h(\bar{\phi}_Z)) - \lambda_{EC} - 2\log_2 \frac{1}{2\epsilon_{PA}} - \log_2 \frac{2}{\epsilon_{cor}} \right] / N_{sum} \quad (4)$$

where $N_{R,nmp}^Z$ and $\bar{\phi}_Z$ are the lower and upper bounds, respectively, of received raw keys due to the non-multiphoton emissions from the source, and the phase error in the Z basis used for the key generation. $h(\cdot)$ is the binary Shannon entropy. λ_{EC} is the lower bound of information leakage during the error correction. ϵ_{PA} and ϵ_{cor} are the security parameter over the error verification, and failure probability of privacy amplification, respectively. N_{sum} is the size of the key block sent out from the encoder. Details about the system parameters and the calculation model are provided in the Methods section.

The QBER is extracted from the sifted raw keys to estimate the SKR, as presented in Fig. 3a, using base comparison of the statistical histograms. The decoder measures the 16 statistical histograms of the detected photons corresponding to the time-bin states repeatedly sent by the encoder. The QBER for each basis is calculated using the statistical ratio of the integrated photon counts at the two perpendicular bases. For example, the QBER for encoded E_{Z_1} is calculated as $N_{Z_0}/N_{Z_0}+N_{Z_1}$, where $\{N_{Z_0}, N_{Z_1}\}$ are the integrated photon counts within each 4.3 ns time windows $\{W3, W1\}$ of the histograms (Bit no. 2, 5, 8, 12, 15, 16). Same calculation algorithm applies to E_{Z_0} , which is $N_{Z_1}/N_{Z_0}+N_{Z_1}$ with $\{N_{Z_0}, N_{Z_1}\}$ counted within the time window $\{W3, W1\}$ from the corresponding histograms (Bit no. 3, 5, 9, 11, 14). However, determining E_{X_0} is relatively challenging due to the absence of one more detector channel of $AMZI_2$ for the N_{X_0} and N_{X_1} at the same time. We adjust PS phase to be $-\pi/2$ while sending the $|X_0\rangle$, such that theoretically there is no correlation peak within the W_2 window from the $|X_0\rangle$ state due to the destructive interference. Then, we regard the detected error qubits as N_{X_1} similar as four-state BB84 protocol, and assume the QBER of $|X_0\rangle$ state to be $E_{X_0} = N_{X_1}/N_{Z_0}+N_{Z_1}$, as the splitting ratio between X- and Z- basis at the decoder is $1/2$ resulting in $N_{X_0} + N_{X_1} = N_{Z_0} + N_{Z_1}$ (Bit no. 1, 4, 7, 10, 13). For the measurement of E_{X_0} , the phase difference between the paths of $AMZI_2$ is dynamically stabilized by suppressing the photon counts N_{X_1} within the time window W_2 to be the minimal.

To investigate the stability of the time-bin QKD system in terms of the QBER, SKBs per pulse at different quantum channel lengths, we implement the time-dependent measurement using the length-variable fiber spools (average loss of $\alpha = 0.1956 \text{ dB km}^{-1}$) connected between the transmitter and receiver setups. As shown in Fig. 3b, the mean and deviation of QBERs at X basis are both relatively higher than Z basis, due to the limited single-photon interference visibility of $|X_0\rangle$ state at the BS_4 . We attribute the slightly higher QBERs of $|Z_1\rangle$ state compared to the $|Z_0\rangle$ state to the imperfect phase encoding of PM due to inaccurate targeting voltage (i.e., flatness uncertainty of the peak voltage). In fact, a fast tuning of the voltage V_π is applied in a single-photon period to generate $|Z_1\rangle$ state, but no tuning action is required for the $|Z_0\rangle$ state. The QBER increases with the length of the optical fiber, since the system dark counts become more dominant with a decreased signal-to-noise ratio. Nevertheless, average QBERs below 11 % are maintained at a transmission distance of 120 km, which is promising for a secure intercity-scale communication. Figure 3c illustrates stable SKB per pulse over 6 hours for different fiber spools, which is the ratio of R_{secure} and f_{rep} . The average E_{X_0} within the integration time is dynamically employed in the calculation of R_{secure} , while considering fixed values of the mean photon number per pulse $\langle n \rangle = 2.89 \times 10^{-3}$ entering the quantum channel and $g^{(2)}(0) = 0.85 \%$. The integrated finite blocks at a distance of 120 km are given a longer time of 20 min to ensure sufficient key length for a positive key rate.

Table 1 presents the statistics of the Gaussian distribution according to the results from Fig. 3. The extraction ratio of the R_{secure} from the raw key rate R_{raw} becomes lower with the enhanced transmission distance because of the increased QBER. With the case of the repetition rate $f_{rep} = 75.947 \text{ MHz}$, the reachable SKR at the distance of 120 km is approx. 15 bits s^{-1} , which is still possible for the text message encryption. The standard deviation of the QBERs ($\sigma_{\{Z_0, Z_1, X_0\}}$) on both the Z- and X-bases remains below 0.6 % to be constant thanks to the effective phase compensation program and stable laboratory environment. Fig. 4(a) presents the QBERs, the SKB per pulse as a function of the transmission distance. Apart from the

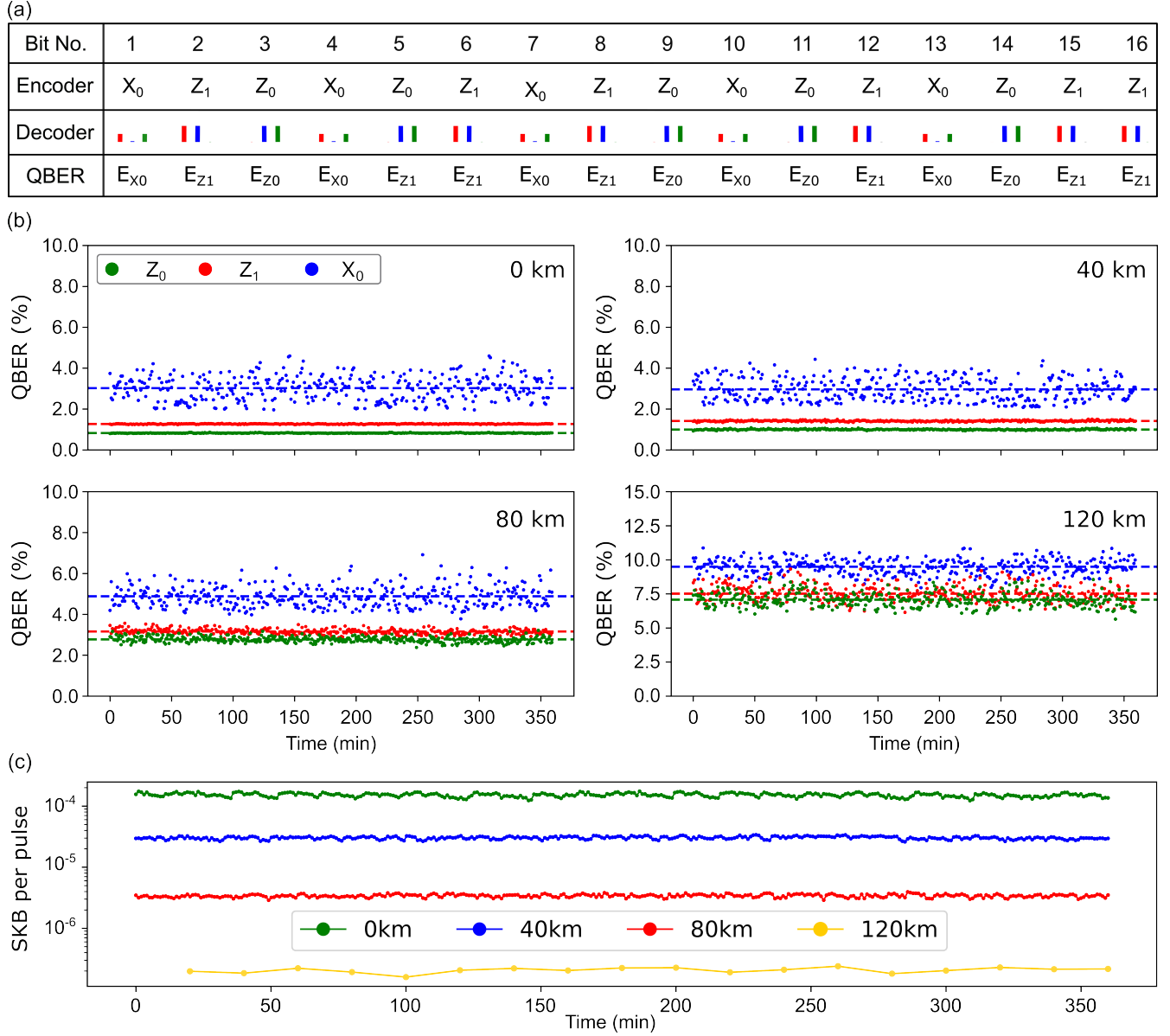


Figure 3. (a) Schematic of QBER extraction with the bases comparison of statistical data. The time windows $\{W1, W2, W3\}$ are indicated by the red, blue, and green columns, respectively. The height of each columns denotes the probability of detecting photons within a given time window when specific states are encoded. (b) Time-dependent QBER for different fiber pool lengths of 0 km, 40 km, 80 km, and 120 km. Each data point represents 1 min of measurement time. The dashed lines indicate the average QBERs on the bases over the 6 hours. (c) Secure key bits (SKBs) per pulse as a function of measurement time for the different fiber pool lengths ranging from 0 km to 120 km. For the pool lengths of 0 km, 40 km, and 80 km, an acquisition time of 1 min ($N_{sum} = 4.56 \times 10^9$) is used in the finite key analysis. For the 120 km transmission distance, an acquisition time of 20 min ($N_{sum} = 9.12 \times 10^{10}$) is used.

Distance (km)	$R_{\text{secure}}/f_{\text{rep}}$	$R_{\text{raw}}/f_{\text{rep}}$	E_Z (%)	σ_{Z_0} (%)	σ_{Z_1} (%)	E_{X_0} (%)	σ_{X_0} (%)
0	1.59×10^{-4}	2.23×10^{-4}	0.98%	0.01%	0.01%	3.14%	0.54%
40	3.04×10^{-5}	4.33×10^{-5}	1.19%	0.08%	0.03%	3.12%	0.56%
80	3.54×10^{-6}	6.87×10^{-6}	3.02%	0.13%	0.14%	4.90%	0.52%
120	1.99×10^{-7}	1.34×10^{-6}	6.85%	0.60%	0.56%	9.60%	0.58%

Table 1. SKB per pulse and QBERs over a range of fiber spool lengths. The QBER on Z-basis, E_Z , is the average value of E_{Z_0} and E_{Z_1} . Acquisition times of 1 min and 20 min with the key blocks in the finite key regime are used for 0~80 km and 120 km, respectively.

experimental data points as illustrated in the above table, we performed a simulation to determine the maximum tolerable distance for our time-bin QKD system, where the QBERs of E_X and E_Z on Z- and X-bases (ϕ^Z and ϕ^X) are simulated as,

$$E_X = \frac{M_R^X}{N_{R,nmp}^X} \quad E_Z = \frac{M_R^Z}{N_{R,nmp}^Z} \quad (5)$$

where $M_R^{X,Z}$ and $N_{R,nmp}^{X,Z}$ denote the number of error bits and lower bound of non-multiphoton fraction of received photons at $\{X, Z\}$ bases, respectively (see Methods for details). A maximum tolerable distance of 127 km is underestimated in the case that the QBER at X-basis approaches 11 %, since keys from Z-basis with a lower QBER value is typically employed for the information encryption in practical QKDs.

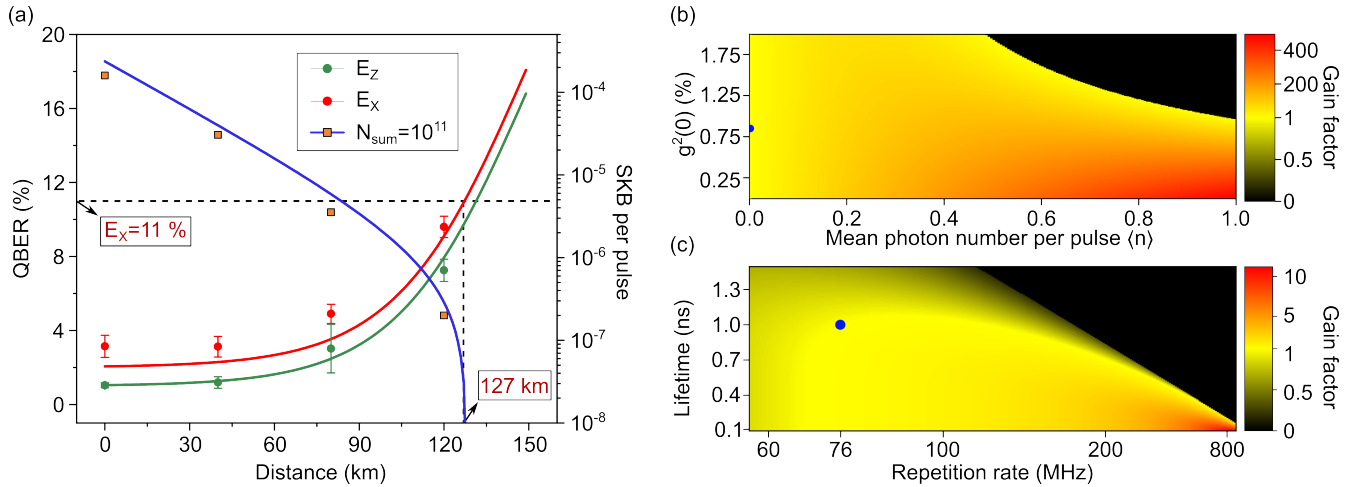


Figure 4. (a) QBERs at the $|X\rangle$ and $|Z\rangle$ bases and SKB per pulse as a function of the secret key transmission distance. A received block size of $N_{\text{sum}} = 10^{11}$ is employed for the finite key analysis. (b) Gain of simulated SKR as a function of the mean photon number per pulse $\langle n \rangle$ and second order autocorrelation $g^{(2)}(0)$, compared with this experiment. (c) Gain of simulated SKR as a function of the repetition rate of the excitation laser and the QD lifetime, compared with this experiment. The blue circles indicate the parameters in the current time-bin QKD system.

Discussion

In our experiment, a secure key rate of 1.99×10^{-7} bit per pulse was achieved over a 120 km fiber spool using a total pulse block size of $N_{\text{sum}} = 10^{11}$, corresponding to an integration time of approximately 1300 s. This result demonstrates the feasibility of employing a deterministic, telecom-band quantum dot single-photon source in a time-bin encoded QKD system under long-distance transmission and realistic conditions. Nevertheless, there remains considerable potential for further improvement in system performance, as discussed below:

1. Influence of source brightness and system loss. The mean photon number $\langle n \rangle$ is a critical parameter affecting the key rate. Increasing source brightness and reducing encoder loss can significantly enhance $\langle n \rangle$ compared to current experimental conditions. As shown in Fig. 4(b), the SKR improves with larger $\langle n \rangle$. However, higher brightness increases sensitivity to multi-photon components, and a low $g^{(2)}(0)$ becomes increasingly important to preserve security. Poor single-photon purity (i.e., high $g^{(2)}(0)$) has a stronger negative impact at higher source brightness.

2. Repetition rate limitations imposed by QD lifetime and modulation structure. Compared with weak coherent laser pulses, quantum dot sources typically exhibit longer radiative lifetimes. Therefore, increasing the system repetition rate leads to temporal overlap between \odot and \ominus wave packets within the Sagnac interferometer (SNI). This overlap region exhibits the same phase and thus lacks modulation contrast, making it unusable for key generation. Additionally, at higher repetition rates, overlap between detection windows (W1, W2, and W3) may occur, resulting in photons from adjacent bits falling into incorrect time bins and increasing the quantum bit error rate (QBER). To further explain this point, we performed simulations based on a fitted model of the quantum dot lifetime to explore the trade-off between repetition rate and temporal overlap, as shown in Fig. 4(c). While higher repetition rates can theoretically enhance the key rate, they are only effective when the pulse lifetime is sufficiently short to prevent peak overlap. An optimal operating point must balance increased repetition with minimal temporal crosstalk.

3. Optical loss in the encoding and decoding modules. The secure key rate is also constrained by the intrinsic loss in both Alice's and Bob's modules. Several components in the system can be optimized further, such as using lower-loss fiber devices and replacing standard fiber connectors with high-precision fusion splicing, thereby minimizing insertion loss and back-reflection.

4. Detector performance and dark count suppression. The performance of the SNSPD plays a crucial role in system reliability. Although the detectors used in this work exhibit good efficiency and low dark count probability, further improvements are possible. Enhancing detector efficiency and reducing background counts through improved device fabrication and environmental isolation could boost the overall key rate.

Conclusion

In summary, we have demonstrated the feasibility and long-term self-stability of a time-bin encoded QKD system based on a deterministic single-photon source at telecom wavelengths. The system operates continuously for over 6 hours at 120 km, achieving a highest finite-size key rate among the time-bin QKDs with single-photon sources. Our work identifies key advantages and also limitations of quantum dot single photon sources for the generation of time-bin qubits. The results provide practical paths for optimization of all system components, therefore contributing to the realization of a robust and scalable quantum communication infrastructure based on solid-state single-photon emitters.

Note added in proof: During the preperation of manuscript, we noticed a similar work by Zhang *et al.*⁶². The authors demonstrated time-bin QKD using a GaN-based quantum dot source. In contrast, our system operates with a InGaAs-based quantum dot source with much higher brightness, achieving higher secure key rates over longer distances (120 km vs. 33 km). Our QKD setup also demonstrates remarkable long-term system stability, a key to a practical QKD infrastructure.

Methods

Transformation of quantum states with the AMZI

For an asymmetric Mach-Zehnder interferometer (AMZI), consisting of two beam splitters and a phase shifter (fast axis along with H polarisation of single photons) for one arm, the transformation matrix for the single-photon states before the BS_4 is,

$$\begin{aligned} R'_{AMZI} &= R_{PS} \otimes R_{BS_3} \\ &= \begin{pmatrix} e^{i\theta_2} & 0 \\ 0 & 1 \end{pmatrix}_{PS} \otimes \frac{1}{\sqrt{2}} \begin{pmatrix} i & 1 \\ 1 & i \end{pmatrix}_{BS_3} \end{aligned} \quad (6)$$

where the R_{BS} , R_{PS} are the transformation matrix for the BS and PS, respectively. Taking into account the single-photon state from the quantum channel is,

$$\begin{aligned} |\Psi\rangle_{AMZI_1} &= \frac{1}{\sqrt{2}} e^{i\frac{\theta_1}{2}} \left(\sin \frac{\theta_1}{2} \cdot |e\rangle + i \cos \frac{\theta_1}{2} \cdot |l\rangle \right) \\ &= \frac{1}{\sqrt{2}} e^{i\frac{\theta_1}{2}} \cdot \begin{pmatrix} \sin \frac{\theta_1}{2} \\ i \cos \frac{\theta_1}{2} \end{pmatrix}_T \otimes \begin{pmatrix} 1 \\ 0 \end{pmatrix}_P \end{aligned} \quad (7)$$

with the first two terms the time-bin states T for the $|e\rangle$ and $|l\rangle$ photons from the quantum channel. The third term indicates the path states P corresponding to $|S\rangle$ and $|L\rangle$ before $AMIZ_2$. The single-photon states before BS_4 is then,

$$\begin{aligned} |\Psi'\rangle_{AMZI_2} &= R'_{AMIZ} \cdot |\Psi\rangle_{AMZI_1} \\ &= \frac{1}{\sqrt{2}} e^{i\frac{\theta_1}{2}} \cdot \left(\sin \frac{\theta_1}{2} \right)_T \otimes \frac{1}{\sqrt{2}} \begin{pmatrix} ie^{i\theta_2} \\ 1 \end{pmatrix}_P \\ &= \frac{1}{2} e^{i\frac{\theta_1}{2}} \cdot \left(i \sin \frac{\theta_1}{2} e^{i\theta_2} \cdot |e, S\rangle + \sin \frac{\theta_1}{2} \cdot |e, L\rangle - \cos \frac{\theta_1}{2} e^{i\theta_2} \cdot |l, S\rangle + i \cos \frac{\theta_1}{2} \cdot |l, L\rangle \right) \end{aligned} \quad (8)$$

In our experiment, only one output port of BS_4 is used for the measurement. The final state from one port of the $AMZI_2$ can be written as follows, with a amplitude factor of $1/\sqrt{2}$ is applied considering the splitting probability of 50:50 with the BS. In addition, assuming that the output of BS_4 corresponds to photons from the short path, it leads to a phase shift of $\pi/2$ with the $|S\rangle$ -state photons sigified by i .

$$|\Psi'\rangle_{AMZI_2} \rightarrow |\Psi\rangle_{AMZI_2} = \frac{1}{2\sqrt{2}} e^{i\frac{\theta_1}{2}} \cdot \left(-\sin \frac{\theta_1}{2} e^{i\theta_2} \cdot |e, S\rangle + \sin \frac{\theta_1}{2} \cdot |e, L\rangle - i \cos \frac{\theta_1}{2} e^{i\theta_2} \cdot |l, S\rangle + i \cos \frac{\theta_1}{2} \cdot |l, L\rangle \right) \quad (9)$$

Estimation of QBERs

In our time-bin QKD system, we estimate the QBERs and SKRs based on the calculation of click $p_{click}^{X,Z}$ and error $p_e^{X,Z}$ probability with the detected photons by SNSPD at $\{X, Z\}$ bases, taking into account of the system parameters such as mean photon number per pulse $\langle n \rangle$, $g^{(2)}(0)$, total system loss (incl. fiber spools) η_{total} , etc.

$$\begin{aligned} p_c^{X,Z} &= \sum_{n=0}^{\infty} p_n [1 - (1 - p_{dc})(1 - \eta_{total})^n] \\ p_e^{X,Z} &= p_0 p_{dc} + \sum_{n=1}^{\infty} p_n [1 - (1 - p_{dc})(1 - \eta_{total})^n] p_{mis} \end{aligned} \quad (10)$$

in which p_{dc} is dark count probability equal to the multiplication of system dark counts d and individual time window $\tau_w = 4.3$ ns. Here, the parameter $p_{mis}^{X,Z}$ is the error probability of the signal components due to imperfect state preparation, channel decoherence, and imperfect power splitting at decoder. This is given by the average QBER for an optical fiber length of 0 km in the experiment. The probability of n -photon emission p_n is calculated as³¹,

$$p_2 = \frac{\bar{n}^2 \cdot g^{(2)}(0)}{2}, \quad p_1 = \bar{n} - 2p_2, \quad p_0 = 1 - p_1 - p_2 \quad (11)$$

with $\bar{n} = \langle n \rangle \cdot \eta_B \cdot \eta_D$ the average photon number per pulse after the detector. In the simulation of Fig. 4 about the QBER as a function of transmission distance, we employ the phase error rate to estimate the QBER in the finite key length regime,

$$E_X = \phi^Z = \frac{M_R^X}{N_{R,nmp}^X} \quad E_Z = \phi^X = \frac{M_R^Z}{N_{R,nmp}^Z} \quad (12)$$

in which $M_R^{X,Z}$ and $N_{R,nmp}^X$ are calculated as,

$$\begin{aligned} M_R^{X,Z} &= N_{sum} \cdot p_{X,Z}^A \cdot p_{X,Z}^B \cdot p_e^{X,Z} \\ N_{R,nmp}^X &= N_R^{X,Z} - \bar{N}_{sum,mp}^{X,Z} \\ &= N_{sum} \cdot p_{X,Z}^A \cdot p_{X,Z}^B \cdot p_c^{X,Z} - N_{sum} \cdot p_{X,Z}^A \cdot p_{X,Z}^B \cdot p_m \end{aligned} \quad (13)$$

$p_{X,Z}^{A,B}$ is the splitting ratio of the keys for the $\{X, Z\}$ bases at the encoder and decoder sites. p_m is the the multi-photon emission probability of the source, which is equal to p_2 in our case by only taking into account the multi-photon events up to two. $\bar{N}_{sum,mp}^{X,Z}$ denote the upper bound of the emitted photons from the encoder that is derived with the upper Chernoff bound and $N_{sum,mp}^{X,Z}$,

$$\bar{x} = (1 + \delta_U) x^* \quad (14)$$

with $\delta^U = \frac{\beta + \sqrt{8\beta x^* + \beta^2}}{2x^*}$ and $\beta = -\log_e(\epsilon_{PE})$.

Calculation of SKR

The calculation of SKR in finite key regime based on the Chernoff bound has been discussed in the previous publications for the polarization-encoded QKDs^{31,41},

$$R_{secure} = \left\lfloor \frac{N_{R,nmp}^Z (1 - h(\bar{\phi}_Z)) - \lambda_{EC} - 2 \log_2 \frac{1}{2\epsilon_{PA}} - \log_2 \frac{2}{\epsilon_{cor}}}{N_{sum}} \right\rfloor \quad (15)$$

with $\bar{\phi}_Z$ calculated as,

$$\begin{aligned} \bar{\phi}_Z &= \phi_Z + \gamma^U \left(N_{R,nmp}^X, N_{R,nmp}^Z, \phi_Z, \frac{\epsilon_{sec}}{6} \right), & \phi_Z = E_X &= \frac{M_R^X}{N_{nmp}^X} \\ \gamma^U(n, k, \lambda, \epsilon') &= \frac{1}{2 + 2 \frac{A^2 G^2}{(n+k)^2}} \left\{ \frac{(1-2\lambda)AG}{n+k} + \sqrt{\frac{A^2 G^2}{(n+k)^2} + 4\lambda(1-\lambda)G} \right\} \\ A &= \max\{n, k\}, & G &= \frac{n+k}{nk} \log_e \frac{n+k}{2\pi n k \lambda (1-\lambda) \epsilon'^2}, \end{aligned} \quad (16)$$

λ_{EC} is the estimation on the known leakage of information from the error correction process,

$$\lambda_{EC} = \left\lfloor n_R^Z (1 - E_Z) - F^{-1} \left(\epsilon_{cor} \cdot \left(1 + \frac{1}{\sqrt{n_R^Z}} \right); n_R^Z, 1 - E_Z \right) - 1 \right\rfloor, \quad (17)$$

where $E_Z = \frac{M_R^Z}{N_R^Z}$ is bit error rate of received Z basis count and $F^{-1} \left(\epsilon_{cor} \left(1 + \frac{1}{\sqrt{n_R^Z}} \right); n_R^Z, 1 - E_Z \right)$ is the inverse of the cumulative distribution function of the binomial distribution. The simulation parameter is displayed in the following Table.2.

Table 2. System Parameters

Description	Parameter	Value
Repetition rate	f_{rep}	75.947 MHz
Average photon number per pulse before the quantum channel	$\langle n \rangle$	2.89×10^{-3}
Second-order correlation	$g^{(2)}$	0.85%
Transmission efficiency of encoder and decoder	η_A, η_B	10.11%, 41.7%
Z-basis choice (Encoder)	p_Z^A	11/16
X-basis choice (Encoder)	p_X^A	5/16
Z- and X- basis choice (Decoder)	p_X^B	1/2
Misalignment probability of Z-basis	p_{misZ}	1%
Misalignment probability of X-basis	p_{misX}	2%
Averaged fibre-spool loss	α	$0.1956 \text{ dB km}^{-1}$
Detector efficiency	η_D	74%
Dead time	τ_{dt}	35.8 ns
Time window of one bit	τ_W	4.3 ns
Dark count probability	p_{dc}	1.33×10^{-6}
Parameter estimation failure probability	ϵ_{PE}	$2 \times 10^{-10}/3$
Error correction failure probability	ϵ_{EC}	$10^{-10}/6$
Privacy amplification failure probability	ϵ_{PA}	$10^{-10}/6$
Error verification failure probability	ϵ_{cor}	10^{-15}

Data availability

The data that support the plots within this paper and other findings of this study are available from the corresponding author upon reasonable request.

Acknowledgements

The authors thank Alessandro Fedrizzi and Frederik Brooke Barnes for the fruitful discussion about SKR simulation, Johann Dzeik for helping with the 3D-printing of encoder and decoder container, and Jialiang Wang for the experimental assistance. The authors gratefully acknowledge the funding by the German Federal Ministry of Education and Research (BMBF) within the project QR.X (16KISQ013 and 16KISQ015), QR.N (16KIS2188 and 16KIS2207), SQuaD (16KISQ117) and SemiQON (13N16291), the European Research Council (MiNet GA101043851). We thank the project EQSOTIC within the QuantERA II Programme that has received funding support from the European Union's Horizon 2020 research and innovation programme under the Grant Agreement No. 101017733, and BMBF (No. 16KIS2060K), the Deutsche Forschungsgemeinschaft (DFG, German Research Foundation) via the Project 469373712, GRK2642, InterSync (GZ: INST 187/880-1 AOBJ: 683478), and under Germany's Excellence Strategy (EXC-2123) Quantum Frontiers (390837967).

Conflict of interest

The authors declare no competing interests.

Author contributions

J.P. Wang built encoder and decoder setup and carried out the QKD experiment (CRediT: Investigation), with help of J. Hanel and X.Y. Cao (CRediT: Methodology). Z.H. Jiang and J.Z. Yang implemented the optical characterization of the quantum dot sample (CRediT: Validation), with preliminary support from M. Jetter and R. Joos (CRediT: Resources). E.P. Rugeramiabo provided support with instrumentation and optical experiments (CRediT: Resources). J.P. Wang performed the data analysis (CRediT: Software). J.P., J. Yang and F. Ding wrote the manuscript (CRediT: Formal analysis, Writing), with the help of S.L. Portalupi, M. Zopf and the other co-authors (CRediT: Project administration, Writing). F. Ding and J.Z. Yang conceived and supervised the project (CRediT: Funding acquisition, Conceptualization, Supervision), with support from S. L. Portalupi and P. Michler (CRediT: Validation, Writing).

References

1. Shor, P. W. & Preskill, J. Simple proof of security of the bb84 quantum key distribution protocol. *Phys. Rev. Lett.* **85**, 441–444, DOI: [10.1103/PhysRevLett.85.441](https://doi.org/10.1103/PhysRevLett.85.441) (2000).
2. Li, H.-W. *et al.* Randomness determines practical security of bb84 quantum key distribution. *Sci. reports* **5**, 1–8 (2015).
3. Lo, H.-K., Chau, H. F. & Ardehali, M. Efficient quantum key distribution scheme and a proof of its unconditional security. *J. Cryptol.* **18**, 133–165 (2005).
4. Scarani, V. & Renner, R. Quantum cryptography with finite resources: Unconditional security bound for discrete-variable protocols with one-way postprocessing. *Phys. Rev. Lett.* **100**, 200501, DOI: [10.1103/PhysRevLett.100.200501](https://doi.org/10.1103/PhysRevLett.100.200501) (2008).
5. *Quantum cryptography: Public key distribution and coin tossing.*
6. Xu, F., Ma, X., Zhang, Q., Lo, H.-K. & Pan, J.-W. Secure quantum key distribution with realistic devices. *Rev. Mod. Phys.* **92**, 025002, DOI: [10.1103/RevModPhys.92.025002](https://doi.org/10.1103/RevModPhys.92.025002) (2020).
7. Gisin, N., Ribordy, G., Tittel, W. & Zbinden, H. Quantum cryptography. *Rev. Mod. Phys.* **74**, 145–195, DOI: [10.1103/RevModPhys.74.145](https://doi.org/10.1103/RevModPhys.74.145) (2002).
8. Zhang, Q., Xu, F., Chen, Y.-A., Peng, C.-Z. & Pan, J.-W. Large scale quantum key distribution: challenges and solutions. *Opt. Express* **26**, 24260–24273, DOI: [10.1364/OE.26.024260](https://doi.org/10.1364/OE.26.024260) (2018).
9. Lo, H.-K., Ma, X. & Chen, K. Decoy state quantum key distribution. *Phys. Rev. Lett.* **94**, 230504, DOI: [10.1103/PhysRevLett.94.230504](https://doi.org/10.1103/PhysRevLett.94.230504) (2005).
10. Wang, X.-B. Beating the photon-number-splitting attack in practical quantum cryptography. *Phys. Rev. Lett.* **94**, 230503, DOI: [10.1103/PhysRevLett.94.230503](https://doi.org/10.1103/PhysRevLett.94.230503) (2005).
11. Lim, C. C. W., Curty, M., Walenta, N., Xu, F. & Zbinden, H. Concise security bounds for practical decoy-state quantum key distribution. *Phys. Rev. A* **89**, 022307, DOI: [10.1103/PhysRevA.89.022307](https://doi.org/10.1103/PhysRevA.89.022307) (2014).
12. Ma, X., Qi, B., Zhao, Y. & Lo, H.-K. Practical decoy state for quantum key distribution. *Phys. Rev. A* **72**, 012326, DOI: [10.1103/PhysRevA.72.012326](https://doi.org/10.1103/PhysRevA.72.012326) (2005).
13. Liao, S.-K. *et al.* Satellite-to-ground quantum key distribution. *Nature* **549**, 43–47 (2017).

14. Ribezzo, D. *et al.* Deploying an inter-european quantum network. *Adv. Quantum Technol.* **6**, 2200061, DOI: <https://doi.org/10.1002/qute.202200061> (2023). <https://onlinelibrary.wiley.com/doi/pdf/10.1002/qute.202200061>.
15. Chen, Y.-A. *et al.* An integrated space-to-ground quantum communication network over 4,600 kilometres. *Nature* **589**, 214–219 (2021).
16. Cao, Y. *et al.* The evolution of quantum key distribution networks: On the road to the qinternet. *IEEE Commun. Surv. & Tutorials* **24**, 839–894, DOI: [10.1109/COMST.2022.3144219](https://doi.org/10.1109/COMST.2022.3144219) (2022).
17. Paraiso, T. K. *et al.* A photonic integrated quantum secure communication system. *Nat. photonics* **15**, 850–856 (2021).
18. Oesterling, L., Hayford, D. & Friend, G. Comparison of commercial and next generation quantum key distribution: Technologies for secure communication of information. In *2012 IEEE Conference on Technologies for Homeland Security (HST)*, 156–161, DOI: [10.1109/THS.2012.6459842](https://doi.org/10.1109/THS.2012.6459842) (2012).
19. Bozzio, M. *et al.* Enhancing quantum cryptography with quantum dot single-photon sources. *npj Quantum Inf.* **8**, 104 (2022).
20. Wang, Q. *et al.* Experimental decoy-state quantum key distribution with a sub-poissonian heralded single-photon source. *Phys. Rev. Lett.* **100**, 090501, DOI: [10.1103/PhysRevLett.100.090501](https://doi.org/10.1103/PhysRevLett.100.090501) (2008).
21. Pousa, R. G., Oi, D. K. & Jeffers, J. Comparison of non-decoy single-photon source and decoy weak coherent pulse in quantum key distribution. *arXiv preprint arXiv:2405.19963* (2024).
22. Yoshino, K.-i. *et al.* Quantum key distribution with an efficient countermeasure against correlated intensity fluctuations in optical pulses. *npj Quantum Inf.* **4**, 8 (2018).
23. Huang, A. *et al.* Laser-seeding attack in quantum key distribution. *Phys. Rev. Appl.* **12**, 064043, DOI: [10.1103/PhysRevApplied.12.064043](https://doi.org/10.1103/PhysRevApplied.12.064043) (2019).
24. Huang, A., Sun, S.-H., Liu, Z. & Makarov, V. Quantum key distribution with distinguishable decoy states. *Phys. Rev. A* **98**, 012330, DOI: [10.1103/PhysRevA.98.012330](https://doi.org/10.1103/PhysRevA.98.012330) (2018).
25. Trefilov, D. *et al.* Intensity correlations in decoy-state bb84 quantum key distribution systems. *arXiv preprint arXiv:2411.00709* (2024).
26. Arakawa, Y. & Holmes, M. J. Progress in quantum-dot single photon sources for quantum information technologies: A broad spectrum overview. *Appl. Phys. Rev.* **7**, 021309, DOI: [10.1063/5.0010193](https://doi.org/10.1063/5.0010193) (2020). https://pubs.aip.org/aip/apr/article-pdf/doi/10.1063/5.0010193/19741983/021309_1_online.pdf.
27. Lu, C.-Y. & Pan, J.-W. Quantum-dot single-photon sources for the quantum internet. *Nat. Nanotechnol.* **16**, 1294–1296 (2021).
28. Vajner, D. A., Rickert, L., Gao, T., Kaymazlar, K. & Heindel, T. Quantum communication using semiconductor quantum dots. *Adv. Quantum Technol.* **5**, 2100116, DOI: <https://doi.org/10.1002/qute.202100116> (2022). <https://onlinelibrary.wiley.com/doi/pdf/10.1002/qute.202100116>.
29. Couteau, C. *et al.* Applications of single photons to quantum communication and computing. *Nat. Rev. Phys.* **5**, 326–338 (2023).
30. Takemoto, K. *et al.* Quantum key distribution over 120 km using ultrahigh purity single-photon source and superconducting single-photon detectors. *Sci. reports* **5**, 14383 (2015).
31. Morrison, C. L. *et al.* Single-emitter quantum key distribution over 175 km of fibre with optimised finite key rates. *Nat. Commun.* **14**, 3573 (2023).
32. Intallura, P. M. *et al.* Quantum communication using single photons from a semiconductor quantum dot emitting at a telecommunication wavelength. *J. Opt. A: Pure Appl. Opt.* **11**, 054005, DOI: [10.1088/1464-4258/11/5/054005](https://doi.org/10.1088/1464-4258/11/5/054005) (2009).
33. Intallura, P. M. *et al.* Quantum key distribution using a triggered quantum dot source emitting near 1.3 μm . *Appl. Phys. Lett.* **91**, 161103, DOI: [10.1063/1.2799756](https://doi.org/10.1063/1.2799756) (2007). https://pubs.aip.org/aip/apl/article-pdf/doi/10.1063/1.2799756/14381878/161103_1_online.pdf.
34. Gao, T. *et al.* A quantum key distribution testbed using a plug&play telecom-wavelength single-photon source. *Appl. Phys. Rev.* **9**, 011412, DOI: [10.1063/5.0070966](https://doi.org/10.1063/5.0070966) (2022). https://pubs.aip.org/aip/apr/article-pdf/doi/10.1063/5.0070966/19809308/011412_1_online.pdf.
35. Schimpf, C. *et al.* Quantum cryptography with highly entangled photons from semiconductor quantum dots. *Sci. Adv.* **7**, eabe8905, DOI: [10.1126/sciadv.abe8905](https://doi.org/10.1126/sciadv.abe8905) (2021). <https://www.science.org/doi/pdf/10.1126/sciadv.abe8905>.

36. Zahidy, M. *et al.* Quantum key distribution using deterministic single-photon sources over a field-installed fibre link. *npj Quantum Inf.* **10**, 2 (2024).
37. Basset, F. B. *et al.* Daylight entanglement-based quantum key distribution with a quantum dot source. *Quantum Sci. Technol.* **8**, 025002, DOI: [10.1088/2058-9565/acae3d](https://doi.org/10.1088/2058-9565/acae3d) (2023).
38. Rau, M. *et al.* Free space quantum key distribution over 500 meters using electrically driven quantum dot single-photon sources—a proof of principle experiment. *New J. Phys.* **16**, 043003, DOI: [10.1088/1367-2630/16/4/043003](https://doi.org/10.1088/1367-2630/16/4/043003) (2014).
39. Samaner, c., Paçal, S., Mutlu, G., Uyanık, K. v. & Ateş, S. Free-space quantum key distribution with single photons from defects in hexagonal boron nitride. *Adv. Quantum Technol.* **5**, 2200059, DOI: <https://doi.org/10.1002/qute.202200059> (2022). <https://onlinelibrary.wiley.com/doi/pdf/10.1002/qute.202200059>.
40. Nawrath, C. *et al.* Bright source of purcell-enhanced, triggered, single photons in the telecom c-band. *Adv. Quantum Technol.* **6**, 2300111, DOI: <https://doi.org/10.1002/qute.202300111> (2023). <https://onlinelibrary.wiley.com/doi/pdf/10.1002/qute.202300111>.
41. Yang, J. *et al.* High-rate intercity quantum key distribution with a semiconductor single-photon source. *Light. Sci. & Appl.* **13**, 150 (2024).
42. Heindel, T. *et al.* Quantum key distribution using quantum dot single-photon emitting diodes in the red and near infrared spectral range. *New J. Phys.* **14**, 083001, DOI: [10.1088/1367-2630/14/8/083001](https://doi.org/10.1088/1367-2630/14/8/083001) (2012).
43. Al-Juboori, A. *et al.* Quantum key distribution using a quantum emitter in hexagonal boron nitride. *Adv. Quantum Technol.* **6**, 2300038, DOI: <https://doi.org/10.1002/qute.202300038> (2023). <https://onlinelibrary.wiley.com/doi/pdf/10.1002/qute.202300038>.
44. Li, Y. *et al.* High-speed robust polarization modulation for quantum key distribution. *Opt. Lett.* **44**, 5262–5265, DOI: [10.1364/OL.44.005262](https://doi.org/10.1364/OL.44.005262) (2019).
45. Rodimin, V. *et al.* A detailed model for polarization mode dispersion in broadband polarization-encoded qkd. In *Photonics for Quantum 2024*, vol. 13106, 22–31 (SPIE, 2024).
46. Lucio-Martinez, I., Chan, P., Mo, X., Hosier, S. & Tittel, W. Proof-of-concept of real-world quantum key distribution with quantum frames. *New J. Phys.* **11**, 095001, DOI: [10.1088/1367-2630/11/9/095001](https://doi.org/10.1088/1367-2630/11/9/095001) (2009).
47. Agnesi, C., Avesani, M., Stanco, A., Villaresi, P. & Vallone, G. All-fiber self-compensating polarization encoder for quantum key distribution. *Opt. Lett.* **44**, 2398–2401, DOI: [10.1364/OL.44.002398](https://doi.org/10.1364/OL.44.002398) (2019).
48. Ding, Y.-Y. *et al.* Polarization variations in installed fibers and their influence on quantum key distribution systems. *Opt. Express* **25**, 27923–27936, DOI: [10.1364/OE.25.027923](https://doi.org/10.1364/OE.25.027923) (2017).
49. Yin, H.-L. *et al.* Experimental composable security decoy-state quantum key distribution using time-phase encoding. *Opt. Express* **28**, 29479–29485, DOI: [10.1364/OE.401829](https://doi.org/10.1364/OE.401829) (2020).
50. Boaron, A. *et al.* Simple 2.5 ghz time-bin quantum key distribution. *Appl. Phys. Lett.* **112**, 171108, DOI: [10.1063/1.5027030](https://doi.org/10.1063/1.5027030) (2018). https://pubs.aip.org/aip/apl/article-pdf/doi/10.1063/1.5027030/19753557/171108_1_online.pdf.
51. Tanaka, A. *et al.* High-speed quantum key distribution system for 1-mbps real-time key generation. *IEEE J. Quantum Electron.* **48**, 542–550, DOI: [10.1109/JQE.2012.2187327](https://doi.org/10.1109/JQE.2012.2187327) (2012).
52. Tang, Y.-L. *et al.* Measurement-device-independent quantum key distribution over 200 km. *Phys. Rev. Lett.* **113**, 190501, DOI: [10.1103/PhysRevLett.113.190501](https://doi.org/10.1103/PhysRevLett.113.190501) (2014).
53. Tang, B.-Y. *et al.* Free-running long-distance reference-frame-independent quantum key distribution. *npj Quantum Inf.* **8**, 117 (2022).
54. Jin, J. *et al.* Genuine time-bin-encoded quantum key distribution over a turbulent depolarizing free-space channel. *Opt. Express* **27**, 37214–37223, DOI: [10.1364/OE.27.037214](https://doi.org/10.1364/OE.27.037214) (2019).
55. Anderson, M. *et al.* Gigahertz-clocked teleportation of time-bin qubits with a quantum dot in the telecommunication c band. *Phys. Rev. Appl.* **13**, 054052 (2020).
56. Yu, H. *et al.* Quantum key distribution implemented with d-level time-bin entangled photons. *Nat. Commun.* **16**, 171 (2025).
57. Fitzke, E. *et al.* Scalable network for simultaneous pairwise quantum key distribution via entanglement-based time-bin coding. *PRX Quantum* **3**, 020341 (2022).
58. Jayakumar, H. *et al.* Time-bin entangled photons from a quantum dot. *Nat. communications* **5**, 4251 (2014).

59. Chen, H. *et al.* Invited article: Time-bin entangled photon pairs from bragg-reflection waveguides. *APL Photonics* **3** (2018).
60. Lee, J. *et al.* A quantum dot as a source of time-bin entangled multi-photon states. *Quantum Sci. Technol.* **4**, 025011 (2019).
61. Bacco, D. *et al.* Field trial of a three-state quantum key distribution scheme in the florence metropolitan area. *EPJ Quantum Technol.* **6**, 1–8 (2019).
62. Zhang, H. *et al.* Metropolitan quantum key distribution using a gan-based room-temperature telecommunication single-photon source. *arXiv preprint arXiv:2409.18502* (2024).